Saturn's northern aurorae at solstice from HST observations coordinated with Cassini's Grand Finale

L. Lamy[1], R. Prangé[1], C. Tao[2], T. Kim[3], S. V. Badman[4], P. Zarka[1], B. Cecconi[1], W. S. Kurth[5], W. Pryor[6], E. Bunce[7], A. Radioti[8]

[1]LESIA, Obs. de Paris, PSL, CNRS, UPMC, Univ. Paris Diderot, Meudon, France.
[2]National Institute of Information and Communications Technology, Tokyo, Japan.
[3]Center for Space Plasma and Aeronomic Research, University of Alabama, Huntsville, USA.
[4]Department of Physics, Lancaster University, Lancaster, UK.
[5]Department of Physics and Astronomy, University of Iowa, Iowa City, USA.
[6]Department of Science, Central Arizona College, Coolidge, USA.
[7]Department of Physics and Astronomy, University of Leicester, Leicester, UK.
[8]Space Science, Technologies and Astrophysics Research Institute, Liège, Belgium.

Key Points:

- Saturn's northern UV aurorae at solstice were sampled from HST observations coordinated with Cassini's Grand Finale.
- The observed aurorae are highly variable with powerful events, radiating up to 120 GW, controlled by solar wind and planetary rotation.
- The average auroral brightness strongly varies with LT with two maxima at dawn (previously known) and pre-midnight (newly identified).

Corresponding author: L. Lamy, `laurent.lamy@obspm.fr`

Abstract

Saturn's northern far-ultraviolet aurorae have been regularly observed throughout 2017 with the Space Telescope Imaging Spectrograph (STIS) of the Hubble Space Telescope (HST), during northern summer solstice. These conditions provided the best achievable viewing of the northern kronian auroral region for an Earth-based telescope and a maximal solar illumination, expected to maximize the magnetosphere-ionosphere coupling. The HST observations were coordinated with *in situ* measurements along the path of the Cassini spacecraft across auroral field lines during the Grand Finale. In this study, we analyze 24 STIS images concurrently with quasi-continuous Cassini/RPWS measurements of Saturn's Kilometric Radiation and solar wind parameters derived from numerical MHD models. The observed northern aurorae display highly variable auroral components, **down to timescales of minutes**, with a total power ranging from 7 to 124±11 GW. They include a prominent main oval **poleward of** 72° latitude **and shifted by** ∼ 3° **toward the nightside**, which bears clear signatures of the solar wind and planetary rotation control, **unexpectedly frequent** cusp emissions near noon, including **the brightest ever reported event** which radiated 13 ± 1 GW, and a dayside weak secondary oval **situated** around 70° latitude. On average, the northern aurorae display a strong LT dependence with two maxima at dawn and pre-midnight, the latter being attributed to regular nightside injections possibly associated with solstice conditions. **The average aurora also displays clues of a rotational control of the oval's average position, but not of its intensity**. These results provide a reference **frame** to analyze Cassini *in situ* and/or remote measurements, whether simultaneous or not.

1 Introduction

Saturn's aurorae have been intensively observed from Earth over the past decades with the Hubble Space Telescope (HST) in the far-ultraviolet (FUV) mainly using the Space Telescope Imaging Spectrograph (STIS) and the Advanced Camera for Surveys (ACS) [*Grodent*, 2015, and refs therein]. Many of these observations were coordinated with *in situ* and/or remote measurements from the Cassini spacecraft, including its Ultraviolet Imaging Spectrometer (UVIS), during its orbital tour from 2004 to 2017. Recent reviews summarize our current understanding of kronian auroral processes [*Kurth et al.*, 2009; *Badman et al.*, 2015; *Stallard et al.*, in press, and refs therein].

The UV aurorae are the neutral atmospheric response of the prominent H and H_2 species to precipitations of electrons energized in the magnetosphere. The energy of primary electrons, measured by various methods based on spectroscopic HST/STIS and Cassini/UVIS measurements ranges from a few keV to a few tens of keV [*Gustin et al.*, 2017]. The kronian aurorae decompose into a variety of components, tentatively listed by *Grodent* [2015], driven by different acceleration processes and underlying current systems. We hereafter restrict ourselves to four broad categories : **the so-called main oval, noon/post-noon high latitude emissions (polar cusp and bifurcations), the low-latitude secondary oval and the Enceladus footprint.**

The dominant auroral emission is a circumpolar main oval, whose intensity and location significantly vary with time. It was early found to be associated with Saturn's Kilometric Radiation (SKR) [*Kurth et al.*, 2005] and with strong upward field-aligned currents located slightly equatorward of the open-closed field line boundary [*Bunce et al.*, 2008; *Belenkaya et al.*, 2008; *Hunt et al.*, 2015]. It typically radiates a few tens of kilo-Rayleighs (kR, **local photon flux per pixel**) and a few tens of GW (**total power radiated by the whole auroral region**), although differing definitions of these quantities used in the literature prevent us from cross-comparing them **for the purpose of, for example, investigating** seasonal variations. The quiet main oval is a quasi-circular narrow faint ring of emission near 72 − 75° northern latitudes. By contrast, magnetospheric compressions driven by interplanetary shocks trigger bright auroral storms typically lasting for ∼1.5 planetary rotations (1.5× ~**10.7 h**), with a **significant part of the** main oval expanding toward high latitudes [*Prangé et al.*, 2004; *Clarke et al.*, 2005, 2009; *Meredith et al.*, 2014a; *Badman et al.*, 2016]. Longitudinally extended intensifications along the undisturbed oval phased with SKR were alternately related to rotationally-modulated nightside injections [*Jackman et al.*, 2009; *Mitchell et al.*, 2009; *Nichols et al.*, 2010a; *Lamy et al.*, 2013]. The main oval additionally hosts a variety of smaller-scale transient and/or sub-corotating hot spots [*Radioti et al.*, 2009; *Grodent et al.*, 2011; *Meredith et al.*, 2013; *Radioti et al.*, 2015]. On average, its brightness strongly varies with Local Time (LT) with a main maximum at dawn [*Badman et al.*, 2006; *Lamy et al.*, 2009; *Carbary*, 2012], a **peculiarity** of Saturn's aurorae.

Cusp aurorae have also been **occasionally** identified as emissions radiating a few GW and up to 50 kR, varying on timescales of hours, and confined close to noon either along the main oval or poleward of it depending on the orientation of the interplanetary magnetic field [*Gérard et al.*, 2005; *Meredith et al.*, 2014b; *Palmaerts et al.*, 2016; *Kinrade et al.*, 2017]. Such signatures are sometimes associated with duskside bifurcations of the main emission, similarly attributed to dynamical dayside reconnection [*Radioti et al.*, 2011; *Meredith et al.*, 2014b]. A faint secondary oval, ~ 2 kR bright, has additionally been identified on the southern nightside in HST/STIS and then Cassini/UVIS images equatorward of the main one. **This component** appeared as a **few-degrees-wide** ring near −67° southern latitude [*Grodent et al.*, 2010; *Lamy et al.*, 2013; *Radioti et al.*, 2017]. *Grodent et al.* [2010] attributed it to the precipitation of suprathermal electrons from the middle magnetosphere rather than to a field-aligned current system. Finally, a last important auroral feature consists of a spot at the magnetic footprint of the moon Enceladus driven by the planet-satellite interaction. It was identified as a 1 kR bright emission near +64.5° latitude in only three Cassini/UVIS images [*Pryor et al.*, 2011]. HST **failed to detect this spot** so far [*Wannawichian et al.*, 2008].

In the frame of Cassini's Grand Finale, HST/STIS regularly observed Saturn's northern aurorae throughout 2017, during northern summer solstice (reached on 24 May). These conditions offered the best achievable HST viewing of the northern auroral region. They also provided maximal solar illumination (with a sub-solar latitude of 26.73°), i.e. maximal northern ionospheric conductivity and thus maximized ionosphere-magnetosphere coupling through the current systems driving most of the kronian aurorae. The HST observations were carefully coordinated with *in situ* measurements of the Cassini spacecraft within the auroral region, for which they thus provide a frame of interpretation. In this article, we analyze 24 HST/STIS images concurrently with Cassini SKR observations and propagated solar wind (SW) parameters. The dataset is presented in section 2 and analyzed in section 3. Results are then discussed in section 4. Details on the HST data processing and supplementary Figures are provided in the supplementary material.

2 Dataset

2.1 HST/STIS observations

During the Cassini Grand Finale, STIS observed Saturn's FUV auroral emissions during 25 HST orbits distributed throughout 2017. These were scheduled when Cassini was planned to traverse SKR sources, themselves colocated with layers of auroral field-aligned upward currents [*Lamy et al.*, in press]. Each orbit included a single, ~ 44 **min long**, time-tagged exposure. The time-tag mode provides the arrival time of photons recorded on the STIS MAMA (Multi-Anode Microchannel Array) detector at a 125 microsec resolution and thus enables us to track dynamics at timescales shorter than the exposure **(as illustrated in supplementary Figure S1 and Animation S1)**. Out of 25 orbits, 24 acquired 1024×1024 pix images at 0.00247 arcsec.pix^{-1} resolution with the Strontium Fluoride filter F25SrF$_2$ (148 nm central wavelength, 28 nm FWHM) which rejects wavelengths shortward of 128 nm and notably the H Ly-α line. One orbit was also used to slew the northern auroral region with the 0.5 arcsec slit and the G140L grating. In this study, we focus on the analysis of the images, processed and translated into brightnesses and power radiated over the full H_2 bands (**70-180 nm**) as detailed in the supplementary material.

2.2 Cassini/RPWS data and solar wind models

Cassini quasi-continuous observations of the Radio and Plasma Wave Science experiment (RPWS) [*Gurnett et al.*, 2004] were used to monitor the activity of Saturn's Kilometric Radiation measured between a few kHz and occasionally beyond 1000 kHz. We derived both power integrated over 10-1100 kHz and flux densities between 3.5 and 1500 kHz normalized to 1 AU **observing distance** for comparison purposes with previous studies [*Lamy et al.*, 2008]. The normalization assumes a source-observer distance equal to the planet-observer one, an assumption which is less and less valid for closer Cassini-Saturn distances, but fair enough to assess typical intensities. **We also used northern SKR phases, derived as described in [*Lamy*, 2011] from the most recent northern SKR period (**~ 10.8 **h throughout 2017) [*Lamy*, 2017]**.

The **solar wind** (SW) parameters used in this study were numerically propagated from the Earth's orbit out to Saturn with two **magneto-hydrodynamic (MHD)** codes. The Tao 1D model was originally developed for the jovian case [*Tao et al.*, 2005] and later extrapolated **to Saturn's orbit** (e.g. [*Kimura et al.*, 2013]). The Multi-scale Fluid-kinetic Simulation Suite (MS-FLUKSS) [*Pogorelov et al.*, 2014] is a 3D model validated in the outer heliosphere thanks to *in situ* plasma measurements of Ulysses, Voyager and New Horizons [*Kim et al.*, 2016]. The input parameters are, for both models, near-Earth SW *in situ* observations provided by either NASA/GSFC's OMNI 1h averaged data obtained from Wind measurements [*King and Papitashvili*, 2005] and/or Stereo-A measurements instead. The uncertainty depends on the derived parameters and on the angular separation between the Earth and Saturn and gradually increases from opposition. For angular separations less than 90°, which provide a fair coverage of the year through complementary Omni and Stereo-A inputs, the typical uncertainty on the timing of dynamic pressure fronts is estimated to be less than ±35 h, according to previous results from another 1D model [*Zieger and Hansen*, 2008], whose results are not available for this study.

3 Results

3.1 A variety of variable components

Figure 1 displays polar projections of all STIS images, labelled a to x, as a function of LT. Images h-i, j-k, l-m, o-p, q-r, t-v and w-x were acquired along successive HST orbits. The observed aurorae reveal a rich variety of emissions, **with highly variable, down to timescales of minutes (see Figure S1 and Animation S1), localized features** dominated in intensity by the main oval. The latter is an inhomogeneous circumpolar ring of emission generally more intense in the dawn and pre-midnight sectors. It is quasi-circular at 72-73° latitude in its quiet state (images n, u-v) with brightnesses ranging from a few tens of kR down to the $\sim$ 8 **kR noise level (see supplementary material)**. Whenever active, it reaches higher latitudes, often with a left-handed spiral shape (the oval develops counterclockwise from the pole). In image a, the spiral even surrounds the magnetic pole up to extreme $87-88°$ latitudes. The brightest events reached peak brightnesses in excess of 150 kR (images a, l, s). **Overall, half of the STIS images were acquired when the Cassini magnetic footprint simultaneously intercepted auroral emissions** (red curves).

Isolated emission regions regularly observed close to noon, located either poleward of the main oval (images c, e, n, q, s and possibly i, w, yellow arrows) or along it (images f-h, j, orange arrows) are then interpreted as cusp aurorae. The identification of cusp emission in the latter case is more ambiguous as hot spots sub-corotating along the main oval can move through noon from dawn to dusk [*Meredith et al.*, 2013]. These emissions are often associated with duskside bifurcations of the main oval toward high latitudes (images b, e, j-k, n, s, x) accounting for the general left-handed spiral shape of the main emission. **The association between bifurcations**, suggesting dynamical lobe reconnection, and noon spots further supports the interpretation of the latter as cusp emissions. Image s shows the brightest example around 10:30 LT and 84° latitude, **persisting over the 44 min exposure time and variable at timescales of minutes (see Animation S1 and Figure S1)** with unusually large brightnesses exceeding 100 kR, the largest ever reported.

A faint dayside secondary oval equatorward of the main one clearly appears at several occasions within $65 - 72°$ latitude, sometimes in restricted LT sectors (images a, b, l, v, green arrows). While this secondary emission appears distinct from the main one, we cannot exclude that it is actually reminiscent of ancient long-lived structures from the main oval which moved toward low latitudes. Half of these examples correspond to active events when the main oval moved to high latitudes. In image a, this secondary oval appears at $69 - 72°$ quasi-continuously from 06:00 LT (or 00:00 LT for the emission $\leq 70°$) to 18:00 LT, with brightnesses which can exceed 10 kR (the noise level in Fig. 1a is ~8 kR). Interestingly, for this image at least, the Cassini footprint intercepts the secondary oval near 11:00 LT simultaneously with the STIS exposure. Cassini/MAG measurements [*Dougherty et al.*, 2004] of the azimuthal magnetic component simultaneous to image a (see supplementary Figure S2) reveal successive small-scale abrupt gradients consistent with field-aligned current signatures, preceded ~1 h earlier by a large positive gradient indicating a strong upward current layer consistent with the poleward main emission (e.g. [*Bunce et al.*, 2008; *Talboys et al.*, 2009, 2011; *Hunt et al.*, 2014; *Lamy et al.*, in press]).

Finally, we also systematically searched for possible emission at the northern Enceladus footprint (white boxes) but could not identify any signal.

3.2 Transient enhancements and associated drivers

Figure 2a plots the total auroral power radiated by H_2 (see section 2.1) as a function of time, with the individual power values being listed in Figure 1. The total auroral power radiated in the UV range may be easily obtained by adding a 12% contribution from H-Ly$_\alpha$ (*e.g.* [*Lamy et al.*, 2013]). Overall, the radiated power strongly varies with time, with a factor of ~10 between the weakest and the brightest events, weeks apart (s-t), and with a factor of ~2 between consecutive orbits (t-v or w-x). Seven events showing active emissions radiated power larger than 65 GW, the brightest of which reach 124, 93 and 120 ± 11 GW for images a, l and s, resp. The latter includes the bright cusp emission, which radiated 13±0.5 GW.

Solar wind and planetary rotation both control SKR activity, in addition to UV aurorae. While SW-induced magnetospheric compressions trigger global SKR enhancement extending toward low frequencies and lasting for more than a planetary rotation [*Desch*, 1982; *Kurth et al.*, 2005; *Lamy et al.*, 2010; *Bunce et al.*, 2010; *Kurth et al.*, 2016; *Reed et al.*, 2018], short-lasting SKR intensifications occuring close to the phase of regular SKR bursts are **associated** with rotationally-modulated nightside injections [*Jackman et al.*, 2009; *Mitchell et al.*, 2009; *Lamy et al.*, 2013; *Reed et al.*, 2018].

The purpose of Fig. 2 is to assess the origin of the most active aurorae. Fig. 2b-c displays measurements of SKR radiated power and the dynamic spectrum of its flux density, which provide a quasi-continuous proxy of the auroral activity at high temporal resolution. Fig. 2d-e display solar wind propagated velocity and dynamic pressure derived from the models described in section 2.2. Vertical dashed lines mark the timing of HST observations a-x. We can immediately notice that most (if not all) of long-lasting SKR intensifications with extensions toward both low and high frequencies fairly match the arrival of a SW pressure front within error bars. The 5 brightest FUV events a, e, l-m and s (boldface dashed lines), with power ≥75 GW, peak brightnesses ≥150 kR and high latitude emissions, all coincide with such SKR enhancements (zoomed in RPWS dynamic spectra associated with those events are displayed in supplementary Figure S3) and can in turn be identified as SW-driven auroral storms. Precisely, the UV observations were respectively acquired~23, 19, 28-30 and 20 h after the start of their associated SKR enhancement, itself lasting at least ~52, 22, 47 and 32 h with multiple bursts, respectively, so that the HST images diagnosed a late stage of 4 different storms.

In contrast, the 2 consecutive images j-k, with power of ~ 70 GW and peak brightnesses ≥ 80 kR show a main emission confined at usual latitudes with a midnight active region which rotated toward dawn between the 2 images. These were acquired during quiet solar wind conditions at northern SKR phases of 301 and 354°, just before a modest northern SKR burst (see supplementary Figure S3). This SKR burst thus appears roughly consistent with the arrival of the active region to dawn. The auroral episodes j-k therefore suggest a rotationally-driven nightside injection.

3.3 Average aurora at solstice

We now turn to the mean spatial distribution and intensity of Saturn's northern UV aurorae. Figures 3a-b displays average polar projections as a function of LT : panel a displays brightnesses at high spatial resolution and panel b displays brightness iso-contours of the smoothed image instead. **Figures 3c-d display average intensity profiles as a function of LT and latitude**. The average main oval is a circumpolar ring of emissions of a few kR confined within 70 – 80° latitudes. Increasing brightnesses then gradually map to a dusk-to-noon partial ring, with the most intense emissions (the red-shaded area in panel b maps brightnesses ≥ 15 kR) between pre-midnight and dawn.

The main oval expands poleward beyond ~ 80° between 04:00 and 21:00 LT, encompassing polar arcs and spots produced by dawnside auroral storms, noon cusp and duskside bifurcations. The low average brightness of these high latitude emissions illustrates their transient nature. Figure additionally reveals that the average main oval is **shifted** toward the nightside : while the low-latitude boundary **(estimated from the latitudinally-extended blue-shaded 3 kR contour in Figure 3b)** extends down to 70-72° between 18:00 and 06:00 LT **through midnight** (or even below in the pre-midnight sector), it reaches 73-75° instead between 09:00 and 15:00 LT **through noon**, with highest latitudes at 14:00 LT.

This **shift** enables us to distinctly identify an equatorward secondary oval between 67° and 73° **in Figure 3a-b,d**, split from the main oval, with a typical mean brightness of ~2 kR, occasionally exceeding 3 kR (the standard deviations in Fig. 3a-b are ≤1.5 kR). It is pretty remarkable that this secondary oval is detected quasi-continuously from noon to the dawn and dusk sides with roughly homogeneous intensities, which suggest that it primarily consists of steady weak emissions. These characteristics are fairly consistent with the 1.7 kR secondary oval previously identified at −67° southern nightside latitude [*Grodent et al.*, 2010]. Precisely, when taking into account the 2° northern latitudinal shift due to the northern magnetic field offset, the northern **dayside** oval appears at slightly higher latitudes than the **nightside** southern one, in agreement with the nightside **shift** of the main oval.

Figure 3c quantifies the LT dependence of northern aurorae discussed above by plotting the average brightness profile between 70° and 85° latitude (black line), where the emissions are fully visible **at all LT**. It displays two clear distinct peaks at 05:00 LT and 22:00 LT. When building the same Figure with SW-driven auroral storms removed, these peaks remain but are slightly shifted toward 06:30 and 20:30 LT instead.

Finally, we similarly investigated the role of planetary rotation, previously found to modulate the intensity and position of UV aurorae in both hemispheres [*Nichols et al.*, 2010a,b]. Supplementary Figure S4 displays the auroral brightness integrated over 70 – 80° latitudes of each image as a function of northern SKR phase and LT. The dashed line displays a guide meridian indicating an active auroral region rotating at the northern SKR period and reaching 06 : 00 LT at a phase of 0° (*i.e.* at the timing of SKR bursts). In contrast with previous positive results obtained with a similar representation for the southern UV aurorae and southern SKR sources [*Nichols et al.*, 2010a; *Lamy*, 2011; *Lamy et al.*, 2013], no active region can be continuously tracked along or close to this guide meridian. **Supplementary Figures S5a-b displays average polar projections of the aurorae similar to Figures 3a-b but organized as a function of northern SKR phase. The Local Times were transposed into phases again by assuming that SKR maxima occur at the pass of a rotating active region through** 06 : 00 **LT. Figure S5 does not reveal any particular maximum near** 0°**, in agreement with Figure S4. The two maxima observed near 90° and 180° instead are mainly due to the auroral storms identified above. Looking now at the low-latitude boundary of the main emission (yellow contour in Figure S5b), it clearly reaches higher latitudes on the left-hand side (74-75° latitude at 90° phase) than on the right-hand side (72-73° latitude at 180° phase). This latitudinal shift is consistent with that predicted from the tilt of the northern oval when the upward current layer reaches dawn [*Nichols et al.*, 2010b] and therefore suggests a rotational control of the oval's position (and not of its intensity, as already observed between 2011 and 2013 [*Nichols et al.*, 2016]), whose detailed study is beyond the scope of this paper.**

4 Discussion

In the previous section, we described the individual and average properties of the kronian northern aurorae at solstice, some of which are further discussed below.

The peak of northern average auroral brightness at 05:00 LT matches that previously seen with Cassini/UVIS observations [*Carbary*, 2012], although its displacement toward 06:30 when removing auroral storms provides a typical uncertainty linked to the statistics of the dataset. This may account for the difference with the southern average auroral brightness peak found from HST STIS/ACS observations at 09:00 [*Lamy et al.*, 2009] and from Cassini/UVIS data at 06:00 LT [*Carbary*, 2012]. More importantly, the HST observations of 2017 additionally reveal a second peak of comparable amplitude at 20 : 30 − 22 : 00 LT, previously unreported, and strikingly reminiscent of Earth's aurora. This LT sector is also the one where the equatorward latitude of the main oval (isocontours ≥ 3 kR in Fig. 3) minimizes. We thus suggest that this secondary peak arises **either from a better viewing of the nightside sector or from** more frequent nightside injections sampled in the analyzed dataset than in past studies [*Badman et al.*, 2006; *Lamy et al.*, 2009; *Carbary*, 2012], possibly favored under solstice conditions.

In contrast with a clear LT dependence of the auroral intensity, the rotational dynamics do not seem to play a significant role, if we except the moderate brightening phased with the northern SKR seen in the two successive images j-k **and clues of a rotational control of the oval's position**. Instead, the most obvious variability is that induced by large scale auroral storms driven by the SW, for which SKR quasi-continuous observations provide total durations estimated between 22 and 48 h. This largely exceeds the 11 − 21 h range inferred by [*Meredith et al.*, 2013], which explained a typical duration of ∼ 1.5 planetary rotations for the time needed by hot plasma injected from the nightside with a 60% subcorotational motion to complete one rotation. Accounting for the observed durations would require very low sub-corotational rates (from 20 to 50%). Instead, we propose that storms generally do not result from a single magnetospheric compression but from a series of them consistent with the multiple SKR bursts observed along one long event. The peculiar spiral shape observed in image a with extremely high latitudes surrounding the northern magnetic pole finally questions the interpretation of the main emission as a tracer of the open-closed field line boundary **located 1-2° poleward**, in which case the polar cap **would correspond to a very small region around the pole. Analyzing Cassini *in situ* measurements obtained a few hours before image a (namely when the spacecraft sampled the dawnside region poleward of the main oval) is required to adress this question**. The detailed study of another example of UV auroral storm temporally resolved by

Cassini/UVIS and of an SKR long-lasting enhancement consistent with a SW origin is the subject of a companion paper [*Palmaerts et al.*, 2018].

The apparent systematic ∼ 3° nightside **shift in latitude** of the average northern auroral oval, previously unreported to our knowledge, is consistent with the modeled influence of the solar wind flow on the open-closed field line boundary [*Belenkaya et al.*, 2008].

Cusp emissions and bifurcations were very frequently observed, in ∼ 50% of the images. This unusually high occurrence rate is likely related to the magnetosphere/SW configuration reached at solstice. **This scenario** implies enhanced SW-driven mass loading of the magnetosphere, and therefore supports more frequent nightside plasmoid releases/injections. The observation of an unusually bright cusp emission in image s, extended by a duskside bifurcation connecting it to a spiral-shaped main oval and observed during an auroral storm, suggests that it may have been induced by a SW-driven magnetospheric compression as observed at Earth [*Farrugia et al.*, 1995] and similarly proposed at Uranus [*Lamy et al.*, 2017].

The identification of a dayside low latitude emission with $2-3$ kR brightnesses on average (which compare to that previously identified with comparable brightness and latitude on the nightside) imply a steady mechanism able to operate at all longitudes. In addition, it is worth noting that the dayside portion of the oval is not active in all individual images and in half of the cases during auroral storms. This suggests an additional transient activity possibly linked to dayside compression of magnetic field lines. The **previously proposed origin of such emission related to a suprathermal population of electrons in the middle magnetosphere *Grodent et al.* [2010] is called into question** by both this transient activity and by *in situ* magnetic measurements consistent with small-scale field-aligned currents. **These features are alternatively consistent with either ancient long-lived structures of the main emission associated with strong field-aligned currents which moved toward lower latitudes and/or auroral precipitations associated with a secondary current system previously observed within** $68.5-72°$ **latitudes [*Hunt et al.*, 2015]**. The detailed analysis of Cassini plasma measurements during this peculiar event is also necessary to address these questions.

5 Conclusion

In this study, we analyzed 24 HST/STIS images of Saturn's northern aurorae acquired throughout 2017 during northern summer solstice, concurrently with Cassini/RPWS SKR observations and numerically propagated SW parameters. The observed northern aurorae display highly variable auroral components, with a total power ranging from 7 to 124±11 GW. The prominent component is the main oval **observed poleward of 72° and shifted by** ∼ 3° **toward the nightside** which bears clear signatures of the solar wind (4 auroral storms coincident with SKR long-lasting enhancements) and planetary rotation (1 auroral brightening coincident with a regular SKR burst). Recurrent cusp emissions and bifurcations are unexpectedly frequent, in 50% of the images, with an unusually bright cusp emission observed during an auroral storm which radiated 13 ± 1 GW, likely triggered by the SW. The identification of a dayside secondary oval at 70° latitudes, 2 – 3 kR bright on average with some clues of temporal variability brings new constraints to its possible origins. On average, the northern solstice aurorae display a strong LT dependence with two maxima at dawn and pre-midnight, the latter being attributed to regular nightside injections, with **clues of a rotational control of the oval's average position, but not of its intensity**. These results provide a reference **frame** to analyze Cassini *in situ* and/or remote measurements, whether simultaneous (the Cassini footprints intercepted an auroral component in half of the images) or not.

Acknowledgments

The data analyzed in this study are available from the following sources. The UV observations were obtained from the ESA/NASA Hubble Space Telescope (GO program #14811) : the original data can be retrieved from the MAST archive and the processed data from the APIS service hosted by the Paris Astronomical Data Centre at `http://apis.obspm.fr`. The Cassini/RPWS and MAG original data are accessible through the PDS archive at `https://pds.nasa.gov/`. The HFR processed data are available through the LESIA/Kronos database at `http://www.lesia.obspm.fr/kronos`. LL thanks Linda Spilker for her support to the original HST proposal, Fannie Serrano and Pauline Richard, who investigated short-term dynamics of Saturn's aurorae during their internship at LESIA, and Gabby Provan for useful discussions on the inexhaustible topic of kronian magnetospheric periodicities. The French co-authors acknowledge support from CNES and CNRS/INSU programs of Planetology (PNP) and Heliophysics (PNST). SVB was supported by an STFC Ernest Rutherford Fellowship ST/M005534/1. The research at the University of Iowa was supported byÊNASAÊthroughÊContractÊ1415150 with the Jet Propulsion Laboratory.

References

Badman, S. V., S. W. H. Cowley, J.-C. Gérard, and D. Grodent (2006), A statistical analysis of the location and width of Saturn's southern auroras, *Annales Geophysicae*, *24*, 3533–3545, doi:10.5194/angeo-24-3533-2006.

Badman, S. V., G. Branduardi-Raymont, M. Galand, S. L. G. Hess, N. Krupp, L. Lamy, H. Melin, and C. Tao (2015), Auroral Processes at the Giant Planets: Energy Deposition, Emission Mechanisms, Morphology and Spectra, *Space Science Reviews*, *187*, 99–179, doi:10.1007/s11214-014-0042-x.

Badman, S. V., G. Provan, E. J. Bunce, D. G. Mitchell, H. Melin, S. W. H. Cowley, A. Radioti, W. S. Kurth, W. R. Pryor, J. D. Nichols, S. L. Jinks, T. S. Stallard, R. H. Brown, K. H. Baines, and M. K. Dougherty (2016), Saturn's auroral morphology and field-aligned currents during a solar wind compression, *Icarus*, *263*, 83–93, doi:10.1016/j.icarus.2014.11.014.

Belenkaya, E. S., S. W. H. Cowley, S. V. Badman, M. S. Blokhina, and V. V. Kalegaev (2008), Dependence of the open-closed field line boundary in Saturn's ionosphere on both the IMF and solar wind dynamic pressure: comparison with the UV auroral oval observed by the HST, *Annales Geophysicae*, *26*, 159–166, doi:10.5194/angeo-26-159-2008.

Bunce, E., S. W. H. Cowley, D. L. Talboys, M. K. Dougherty, L. Lamy, W. S. Kurth, P. Schippers, B. Cecconi, P. Zarka, C. S. Arridge, and A. J. Coates (2010), Extraordinary field-aligned current signatures in SaturnÕs high-latitude magnetosphere: Analysis of Cassini data during Revolution 89, *J. Geophys. Res.*

Bunce, E. J., C. S. Arridge, J. T. Clarke, A. J. Coates, S. W. H. Cowley, M. K. Dougherty, J.-C. GéRard, D. Grodent, K. C. Hansen, J. D. Nichols, D. J. Southwood, and D. L. Talboys (2008), Origin of Saturn's aurora: Simultaneous observations by Cassini and the Hubble Space Telescope, *Journal of Geophysical Research (Space Physics)*, *113*, A09209, doi:10.1029/2008JA013257.

Carbary, J. F. (2012), The morphology of Saturn's ultraviolet aurora, *Journal of Geophysical Research (Space Physics)*, *117*, A06210, doi:10.1029/2012JA017670.

Clarke, J. T., J.-C. Gérard, D. Grodent, S. Wannawichian, J. Gustin, J. Connerney, F. Crary, M. Dougherty, W. Kurth, S. W. H. Cowley, E. J. Bunce, T. Hill, and J. Kim (2005), Morphological differences between Saturn's ultraviolet aurorae and those of Earth and Jupiter, *Nature*, *433*, 717–719, doi:10.1038/nature03331.

Clarke, J. T., J. Nichols, J. Gérard, D. Grodent, K. C. Hansen, W. Kurth, G. R. Gladstone, J. Duval, S. Wannawichian, E. Bunce, S. W. H. Cowley, F. Crary, M. Dougherty, L. Lamy, D. Mitchell, W. Pryor, K. Retherford, T. Stallard, B. Zieger, P. Zarka, and

Figures/Fig1.pdf

Figure 1. Polar projections of HST/STIS images of northern kronian aurorae obtained in 2017, plotted as a function of LT **(the red meridian indicate noon)**. The $24\times \sim 44$ min-long exposures (labelled a to x) were projected at 1100 km altitude [*Gérard et al.*, 2009]. The light time travel-corrected observing time, the northern SKR phase and the total power radiated in the H_2 bands are provided above each image. Yellow (orange) arrows indicate plausible cusp emissions poleward of (along) the main oval. Green arrows indicate a low-latitude emission. White boxes map to the Enceladus magnetic footprint. The red (gray) curves plot the Cassini magnetic footprint during (±2 h aside) each HST exposure.

B. Cecconi (2009), Response of Jupiter's and Saturn's auroral activity to the solar wind, *J. Geophys. Res.*, *114*(A13), A05,210, doi:10.1029/2008JA013694.

Desch, M. D. (1982), Evidence for solar wind control of Saturn radio emission, *J. Geophys. Res.*, *87*, 4549–4554, doi:10.1029/JA087iA06p04549.

Dougherty, M. K., S. Kellock, D. J. Southwood, A. Balogh, E. J. Smith, B. T. Tsurutani, B. Gerlach, K. Glassmeier, F. Gleim, C. T. Russell, G. Erdos, F. M. Neubauer, and S. W. H. Cowley (2004), The Cassini Magnetic Field Investigation, *Space Science Reviews*, *114*, 331–383, doi:10.1007/s11214-004-1432-2.

Figures/Fig2.pdf

Figure 2. (a) Total auroral power radiated in the H_2 bands. (b) Total SKR power integrated over 10-1100 kHz with a 90 s resolution [*Lamy et al.*, 2008] derived from (c) Cassini/RPWS dynamic spectrum of flux density between 3.5 and 1500 kHz. (d-e) Velocity and dynamic pressure propagated at Saturn by two MHD models (described in section 2.2), using either Omni or Stereo-A data inputs. The double black arrow plots a ±35 h error bar. Boldface portions of colored curves correspond to angular separation between Wind/Stereo-A and Saturn lower than 90°.

Figures/Fig3.pdf

Figure 3. (a) Average of the 24 polar projections displayed in Figure 1, **once smoothed over a 3 pix-wide running box**. (b) Same as (a) **but using a 17 pix-wide running box instead, aimed at maximizing the signal-to-noise at the expense of spatial resolution.** The color scale indicates iso-contours at 3, 7, 11 and 15 kR. These two panels display the average locus and brightness of the circumpolar main oval within $70-85°$ latitude, of noon cusp emissions within or poleward of the main oval and of the equatorward secondary oval, visible near 70° dayside latitudes. (c) Average intensity profiles integrated in latitude between 70° and 85° (black line) encompassing all auroral emissions and between 55° and 65° (gray line) out of any auroral emissions as a function of LT. The average auroral intensity clearly displays two wide maxima at 05:00 and 22:00 LT. **(d) Same as (c) as a function of latitude for successive 02 h-wide LT ranges (colored lines). The main emission is visible at all LT, with distinct high and low latitude emissions mostly visible on the dayside**.

Farrugia, C. J., P. E. Sandholt, S. W. H. Cowley, D. J. Southwood, A. Egeland, P. Stauning, R. P. Lepping, A. J. Lazarus, T. Hansen, and E. Friis-Christensen (1995), Reconnection-associated auroral activity stimulated by two types of upstream dynamic pressure variations: Interplanetary magnetic field $B_z \sim 0$, $B_y << 0$case, *J. Geophys. Res.*, *100*, 21,753–21,772, doi:10.1029/95JA01082.

Gérard, J.-C., E. J. Bunce, D. Grodent, S. W. H. Cowley, J. T. Clarke, and S. V. Badman (2005), Signature of Saturn's auroral cusp: Simultaneous Hubble Space Telescope FUV observations and upstream solar wind monitoring, *Journal of Geophysical Research (Space Physics)*, *110*(A9), A11201, doi:10.1029/2005JA011094.

Gérard, J.-C., B. Bonfond, J. Gustin, J. T. Clarke, J. T. Clarke, D. Bisikalo, and V. Shematovich (2009), Altitude of SaturnÕs aurora and its implications for the characteristic energy of precipitated electrons, *Geophys. Res. Let.*, *36*, L02,202, doi:10.1029/2008GL036554.

Grodent, D. (2015), A Brief Review of Ultraviolet Auroral Emissions on Giant Planets, *Space Science Reviews*, *187*, 23–50, doi:10.1007/s11214-014-0052-8.

Grodent, D., A. Radioti, B. Bonfond, and J.-C. Gérard (2010), On the origin of Saturn's outer auroral emission, *Journal of Geophysical Research (Space Physics)*, *115*(A14), A08219, doi:10.1029/2009JA014901.

Grodent, D., J. Gustin, J.-C. Gérard, A. Radioti, B. Bonfond, and W. R. Pryor (2011), Small-scale structures in Saturn's ultraviolet aurora, *Journal of Geophysical Research (Space Physics)*, *116*(A15), A09225, doi:10.1029/2011JA016818.

Gurnett, D. A., W. S. Kurth, D. L. Kirchner, G. B. Hospodarsky, T. F. Averkamp, P. Zarka, A. Lecacheux, R. Manning, A. Roux, P. Canu, N. Cornilleau-Wehrlin, P. Galopeau, A. Meyer, R. Boström, G. Gustafsson, J. Wahlund, L. Åhlen, H. O. Rucker, H. P. Ladreiter, W. Macher, L. J. C. Woolliscroft, H. Alleyne, M. L. Kaiser, M. D. Desch, W. M. Farrell, C. C. Harvey, P. Louarn, P. J. Kellogg, K. Goetz, and A. Pedersen (2004), The Cassini Radio and Plasma Wave Investigation, *Space Science Reviews*, *114*, 395–463.

Gustin, J., D. Grodent, A. Radioti, W. Pryor, L. Lamy, and J. Ajello (2017), Statistical study of Saturn's auroral electron properties with Cassini/UVIS FUV spectral images, *Icarus*, *284*, 264–283, doi:10.1016/j.icarus.2016.11.017.

Hunt, G. J., S. W. H. Cowley, G. Provan, E. J. Bunce, I. I. Alexeev, E. S. Belenkaya, V. V. Kalegaev, M. K. Dougherty, and A. J. Coates (2014), Field-aligned currents in Saturn's southern nightside magnetosphere: Subcorotation and planetary period oscillation components, *Journal of Geophysical Research (Space Physics)*, *119*, 9847–9899, doi:10.1002/2014JA020506.

Hunt, G. J., S. W. H. Cowley, G. Provan, E. J. Bunce, I. I. Alexeev, E. S. Belenkaya, V. V. Kalegaev, M. K. Dougherty, and A. J. Coates (2015), Field-aligned currents in Saturn's northern nightside magnetosphere: Evidence for interhemispheric current flow associated with planetary period oscillations, *Journal of Geophysical Research (Space Physics)*, *120*, 7552–7584, doi:10.1002/2015JA021454.

Jackman, C. M., L. Lamy, M. P. Freeman, P. Zarka, B. Cecconi, W. S. Kurth, S. W. H. Cowley, and M. K. Dougherty (2009), On the character and distribution of lower-frequency radio emissions at Saturn and their relationship to substorm-like events, *Journal of Geophysical Research (Space Physics)*, *114*(A13), A08211, doi:10.1029/2008JA013997.

Kim, T. K., N. K. Pogorelov, H. A. Zank, G. P. abd Elliott, and D. J. McComas (2016), Modeling the Solar Wind at the Ulysses, Voyager, and New Horizons Spacecraft, *Astrophysical Journal*, *32*(1), 72, doi:10.3847/0004-637X/832/1/72.

Kimura, T., L. Lamy, C. Tao, S. V. Badman, S. Kasahara, B. Cecconi, P. Zarka, A. Morioka, Y. Miyoshi, D. Maruno, Y. Kasaba, and M. Fujimoto (2013), Long-term modulations of Saturn's auroral radio emissions by the solar wind and seasonal variations controlled by the solar ultraviolet flux, *Journal of Geophysical Research (Space Physics)*, *118*, 7019–7035, doi:10.1002/2013JA018833.

King, J. H., and N. E. Papitashvili (2005), Solar wind spatial scales in and comparisons of hourly Wind and ACE plasma and magnetic field data, *Journal of Geophysical Research (Space Physics)*, *110*, A02104, doi:10.1029/2004JA010649.

Kinrade, J., S. V. Badman, E. J. Bunce, C. Tao, G. Provan, S. W. H. Cowley, A. Grocott, R. L. Gray, D. Grodent, T. Kimura, J. D. Nichols, C. S. Arridge, A. Radioti, J. T. Clarke, F. J. Crary, W. R. Pryor, H. Melin, K. H. Baines, and M. K. Dougherty (2017), An isolated, bright cusp aurora at Saturn, *Journal of Geophysical Research (Space Physics)*, *122*, 6121–6138, doi:10.1002/2016JA023792.

Kurth, W. S., D. A. Gurnett, J. T. Clarke, P. Zarka, M. D. Desch, M. L. Kaiser, B. Cecconi, A. Lecacheux, W. M. Farrell, P. Galopeau, J. Gérard, D. Grodent, R. Prangé, M. K. Dougherty, and F. J. Crary (2005), An Earth-like correspondence between Saturn's auroral features and radio emission, *Nature*, *433*, 722–725, doi:10.1038/nature03334.

Kurth, W. S., E. J. Bunce, J. T. Clarke, F. J. Crary, D. C. Grodent, A. P. Ingersoll, U. A. Dyudina, L. Lamy, D. G. Mitchell, A. M. Persoon, W. R. Pryor, J. Saur, and T. Stallard (2009), Auroral processes, in *Saturn from Cassini-Huygens*, pp. 333–374, Springer, New York.

Kurth, W. S., G. B. Hospodarsky, D. A. Gurnett, L. Lamy, M. K. Dougherty, J. Nichols, E. J. Bunce, W. Pryor, K. Baines, T. Stallard, H. Melin, and F. J. Crary (2016), Saturn kilometric radiation intensities during the Saturn auroral campaign of 2013, *Icarus*, *263*, 2–9, doi:10.1016/j.icarus.2015.01.003.

Lamy, L. (2011), Variability of southern and northern SKR periodicities, in *Planetary Radio Emissions VII*, edited by H. O. Rucker, W. S. Kurth, P. Louarn, & G. Fischer, pp. 39–50, Austrian Academy of Sciences Press, Vienna.

Lamy, L. (2017), The Saturnian Kilometric Radiation before the Cassini Grand Finale, in *Planetary Radio Emissions VIII*, edited by G. Fischer, G. Mann, M. Panchenko, & P. Zarka, p. 171Ð190, Austrian Academy of Sciences Press, Vienna.

Lamy, L., P. Zarka, B. Cecconi, R. Prangé, W. S. Kurth, and D. A. Gurnett (2008), Saturn kilometric radiation: Average and statistical properties, *J. Geophys. Res.*, *113*(A12), 7201–+, doi:10.1029/2007JA012900.

Lamy, L., B. Prangé, R., P. Zarka, B. Cecconi, J. Nichols, and J. Clarke (2009), An auroral oval at the footprint of Saturn's kilometric radio sources, colocated with the UV aurorae, *J. Geophys. Res.*, *114*, A10,212, doi:10.1029/2009JA014401.

Lamy, L., P. Schippers, P. Zarka, B. Cecconi, C. S. Arridge, M. K. Dougherty, P. Louarn, N. André, W. S. Kurth, R. L. Mutel, D. A. Gurnett, and A. J. Coates (2010), Properties of Saturn kilometric radiation measured within its source region, *Geophys. Res. Lett.*, *37*, 12,104–+, doi:10.1029/2010GL043415.

Lamy, L., R. Prangé, W. Pryor, J. Gustin, S. V. Badman, H. Melin, T. Stallard, D.-G. Mitchell, and P. C. Brandt (2013), Multispectral simultaneous diagnosis of Saturn's aurorae throughout a planetary rotation, *Journal of Geophysical Research (Space Physics)*, *118*, 4817–4843, doi:10.1002/jgra.50404.

Lamy, L., R. Prangé, K. C. Hansen, C. Tao, S. W. H. Cowley, T. S. Stallard, H. Melin, N. Achilleos, P. Guio, S. V. Badman, T. Kim, and N. Pogorelov (2017), The aurorae of Uranus past equinox, *Journal of Geophysical Research (Space Physics)*, *122*, 3997–4008, doi:10.1002/2017JA023918.

Lamy, L., P. Zarka, B. Cecconi, R. Prangé, W. S. Kurth, G. Hospodarsky, A. Persoon, M. Morooka, J.-E. Wahlund, and G. Hunt (in press), The low frequency source of SaturnÕs Kilometric Radiation , *Science*.

Meredith, C. J., S. W. H. Cowley, K. C. Hansen, J. D. Nichols, and T. K. Yeoman (2013), Simultaneous conjugate observations of small-scale structures in Saturn's dayside ultraviolet auroras: Implications for physical origins, *Journal of Geophysical Research (Space Physics)*, *118*, 2244–2266, doi:10.1002/jgra.50270.

Meredith, C. J., I. I. Alexeev, S. V. Badman, E. S. Belenkaya, S. W. H. Cowley, M. K. Dougherty, V. V. Kalegaev, G. R. Lewis, and J. D. Nichols (2014a), Saturn's dayside ultraviolet auroras: Evidence for morphological dependence on the direction of the upstream interplanetary magnetic field, *Journal of Geophysical Research (Space Physics)*, *119*, 1994–2008, doi:10.1002/2013JA019598.

Meredith, C. J., S. W. H. Cowley, and J. D. Nichols (2014b), Survey of Saturn auroral storms observed by the Hubble Space Telescope: Implications for storm time scales, *Journal of Geophysical Research (Space Physics)*, *119*, 9624–9642, doi:10.1002/2014JA020601.

Mitchell, D. G., S. M. Krimigis, C. Paranicas, P. C. Brandt, J. F. Carbary, E. C. Roelof, W. S. Kurth, D. A. Gurnett, J. T. Clarke, J. D. Nichols, J.-C. Gérard, D. C. Grodent, M. K. Dougherty, and W. R. Pryor (2009), Recurrent energization of plasma in the midnight-to-dawn quadrant of Saturn's magnetosphere, and its relationship to auroral UV and radio emissions, *Planet. Sp. Sci.*, *57*, 1732–1742, doi:10.1016/j.pss.2009.04.002.

Nichols, J. D., B. Cecconi, J. T. Clarke, S. W. H. Cowley, J.-C. Gérard, A. Grocott, D. Grodent, L. Lamy, and P. Zarka (2010a), Variation of Saturn's UV aurora with SKR phase, *Geophys. Res. Lett.*, *371*, L15102, doi:10.1029/2010GL044057.

Nichols, J. D., S. W. H. Cowley, and L. Lamy (2010b), Dawn-dusk oscillation of Saturn's conjugate auroral ovals, *Geophys. Res. Lett.*, *372*, L24102, doi:10.1029/2010GL045818.

Nichols, J. D., S. V. Badman, E. J. Bunce, J. T. Clarke, S. W. H. Cowley, G. J. Hunt, and G. Provan (2016), Saturn's northern auroras as observed using the Hubble Space Telescope, *Icarus*, *263*, 17–31, doi:10.1016/j.icarus.2015.09.008.

Palmaerts, B., A. Radioti, E. Roussos, D. Grodent, J.-C. Gérard, N. Krupp, and D. G. Mitchell (2016), Pulsations of the polar cusp aurora at Saturn, *Journal of Geophysical Research (Space Physics)*, *121*(A10), 11, doi:10.1002/2016JA023497.

Palmaerts, B., A. Radioti, Z. H. Yao, T. J. Bradley, E. Roussos, L. Lamy, E. J. Bunce, S. W. H. Cowley, N. Krupp, W. S. Kurth, E. J. Bunce, J.-C. Gérard, and W. Pryor (2018), Auroral storm and polar arcs at Saturn - Final Cassini/UVIS auroral observations, *Geophysical Research Letters*, p. in press.

Pogorelov, N. V., S. N. Borovikov, J. Heerikhuisen, K. K. Tae, I. A. Kryukov, and G. P. Zank (2014), MS-FLUKSS and Its Application to Modeling Flows of Partially Ionized Plasma in the Heliosphere, in *2014 Annual Conference on Extreme Science and Engineering Discovery Environment*, ACM Digital Library (New York), doi:doi:10.1145/2616498.2616499.

Prangé, R., L. Pallier, K. C. Hansen, R. Howard, A. Vourlidas, R. Courtin, and C. Parkinson (2004), An interplanetary shock traced by planetary auroral storms from the Sun to Saturn, *Nature*, *432*, 78–81, doi:10.1038/nature02986.

Pryor, W. R., A. M. Rymer, D. G. Mitchell, T. W. Hill, D. T. Young, J. Saur, G. H. Jones, S. Jacobsen, S. W. H. Cowley, B. H. Mauk, A. J. Coates, J. Gustin, D. Grodent, J.-C. Gérard, L. Lamy, J. D. Nichols, S. M. Krimigis, L. W. Esposito, M. K. Dougherty, A. J. Jouchoux, A. I. F. Stewart, W. E. McClintock, G. M. Holsclaw, J. M. Ajello, J. E. Colwell, A. R. Hendrix, F. J. Crary, J. T. Clarke, and X. Zhou (2011), The auroral footprint of Enceladus on Saturn, *Nature*, *472*, 331–333, doi:10.1038/nature09928.

Radioti, A., D. Grodent, J.-C. Gérard, E. Roussos, C. Paranicas, B. Bonfond, D. G. Mitchell, N. Krupp, S. Krimigis, and J. T. Clarke (2009), Transient auroral features at Saturn: Signatures of energetic particle injections in the magnetosphere, *Journal of Geophysical Research (Space Physics)*, *114*, A03210, doi:10.1029/2008JA013632.

Radioti, A., D. Grodent, J.-C. Gérard, S. E. Milan, B. Bonfond, J. Gustin, and W. Pryor (2011), Bifurcations of the main auroral ring at Saturn: ionospheric signatures of consecutive reconnection events at the magnetopause, *Journal of Geophysical Research (Space Physics)*, *116*(A15), A11209, doi:10.1029/2011JA016661.

Radioti, A., D. Grodent, J.-C. Gérard, E. Roussos, D. Mitchell, B. Bonfond, and W. Pryor (2015), Auroral spirals at Saturn, *Journal of Geophysical Research (Space Physics)*, *120*, 8633–8643, doi:10.1002/2015JA021442.

Radioti, A., D. Grodent, Z. H. Yao, J.-C. Gérard, S. V. Badman, W. Pryor, and B. Bonfond (2017), Dawn Auroral Breakup at Saturn Initiated by Auroral Arcs: UVIS/Cassini

Beginning of Grand Finale Phase, *Journal of Geophysical Research (Space Physics)*, *122*(A11), 12, doi:10.1002/2017JA024653.

Reed, J. J., C. M. Jackman, L. Lamy, W. S. Kurth, and D. K. Whiter (2018), Low-Frequency Extensions of the Saturn Kilometric Radiation as a Proxy for Magnetospheric Dynamics, *Journal of Geophysical Research (Space Physics)*, *123*, 443–463, doi:10.1002/2017JA024499.

Stallard, T., S. V. Badman, U. Dyudina, D. Grodent, and L. Lamy (in press), Saturn's aurora, in *Saturn in the 21st Century*, pp. 333–374, Cambridge University Press, Cambridge.

Talboys, D. L., C. S. Arridge, E. J. Bunce, A. J. Coates, S. W. H. Cowley, and M. K. Dougherty (2009), Characterization of auroral current systems in Saturn's magnetosphere: High-latitude Cassini observations, *Journal of Geophysical Research (Space Physics)*, *114*, A06220, doi:10.1029/2008JA013846.

Talboys, D. L., E. J. Bunce, S. W. H. Cowley, C. S. Arridge, A. J. Coates, and M. K. Dougherty (2011), Statistical characteristics of field-aligned currents in Saturn's nightside magnetosphere, *Journal of Geophysical Research (Space Physics)*, *116*, A04213, doi:10.1029/2010JA016102.

Tao, C., R. Kataoka, H. Fukunishi, Y. Takahashi, and T. Yokoyama (2005), Magnetic field variations in the Jovian magnetotail induced by solar wind dynamic pressure enhancements, *Journal of Geophysical Research (Space Physics)*, *110*(A9), A11208, doi:10.1029/2004JA010959.

Wannawichian, S., J. T. Clarke, and D. H. Pontius (2008), Interaction evidence between Enceladus' atmosphere and Saturn's magnetosphere, *Journal of Geophysical Research (Space Physics)*, *113*, A07217, doi:10.1029/2007JA012899.

Zieger, B., and K. C. Hansen (2008), Statistical validation of a solar wind propagation model from 1 to 10 AU, *Journal of Geophysical Research (Space Physics)*, *113*(A12), A08107, doi:10.1029/2008JA013046.

Figure 1.

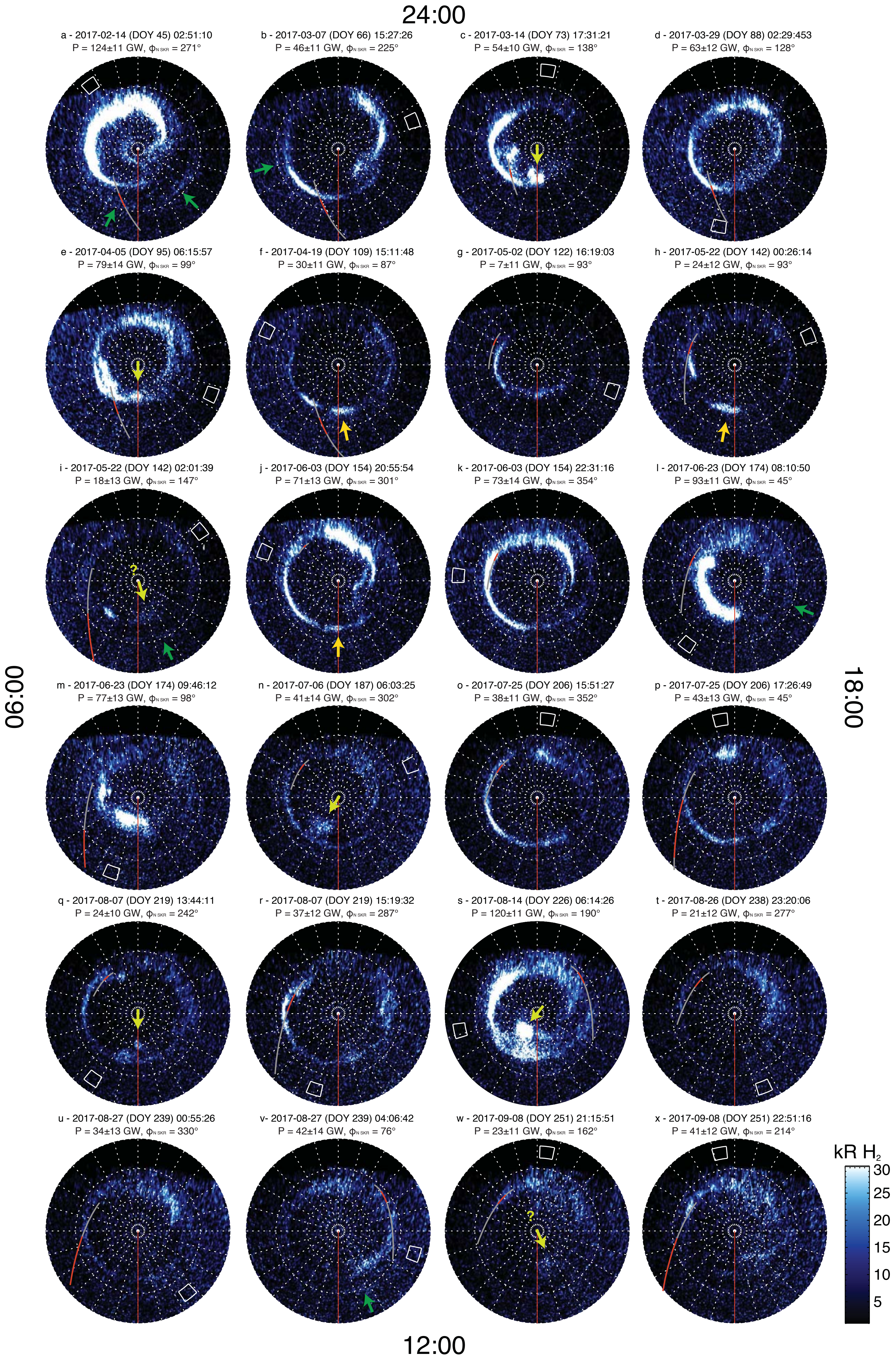
24:00
a - 2017-02-14 (DOY 45) 02:51:10
P = 124±11 GW, ϕN SKR = 271°
b - 2017-03-07 (DOY 66) 15:27:26
P = 46±11 GW, ϕN SKR = 225°
c - 2017-03-14 (DOY 73) 17:31:21
P = 54±10 GW, ϕN SKR = 138°
d - 2017-03-29 (DOY 88) 02:29:453
P = 63±12 GW, ϕN SKR = 128°
e - 2017-04-05 (DOY 95) 06:15:57
P = 79±14 GW, ϕN SKR = 99°
f - 2017-04-19 (DOY 109) 15:11:48
P = 30±11 GW, ϕN SKR = 87°
g - 2017-05-02 (DOY 122) 16:19:03
P = 7±11 GW, ϕN SKR = 93°
h - 2017-05-22 (DOY 142) 00:26:14
P = 24±12 GW, ϕN SKR = 93°
i - 2017-05-22 (DOY 142) 02:01:39
P = 18±13 GW, ϕN SKR = 147°
?
j - 2017-06-03 (DOY 154) 20:55:54
P = 71±13 GW, ϕN SKR = 301°
k - 2017-06-03 (DOY 154) 22:31:16
P = 73±14 GW, ϕN SKR = 354°
l - 2017-06-23 (DOY 174) 08:10:50
P = 93±11 GW, ϕN SKR = 45°
06:00
18:00
m - 2017-06-23 (DOY 174) 09:46:12
P = 77±13 GW, ϕN SKR = 98°
n - 2017-07-06 (DOY 187) 06:03:25
P = 41±14 GW, ϕN SKR = 302°
o - 2017-07-25 (DOY 206) 15:51:27
P = 38±11 GW, ϕN SKR = 352°
p - 2017-07-25 (DOY 206) 17:26:49
P = 43±13 GW, ϕN SKR = 45°
q - 2017-08-07 (DOY 219) 13:44:11
P = 24±10 GW, ϕN SKR = 242°
r - 2017-08-07 (DOY 219) 15:19:32
P = 37±12 GW, ϕN SKR = 287°
s - 2017-08-14 (DOY 226) 06:14:26
P = 120±11 GW, ϕN SKR = 190°
t - 2017-08-26 (DOY 238) 23:20:06
P = 21±12 GW, ϕN SKR = 277°
u - 2017-08-27 (DOY 239) 00:55:26
P = 34±13 GW, ϕN SKR = 330°
v- 2017-08-27 (DOY 239) 04:06:42
P = 42±14 GW, ϕN SKR = 76°
w - 2017-09-08 (DOY 251) 21:15:51
P = 23±11 GW, ϕN SKR = 162°
?
x - 2017-09-08 (DOY 251) 22:51:16
P = 41±12 GW, ϕN SKR = 214°
kR H2
30
25
20
15
10
5
12:00

Figure 2.

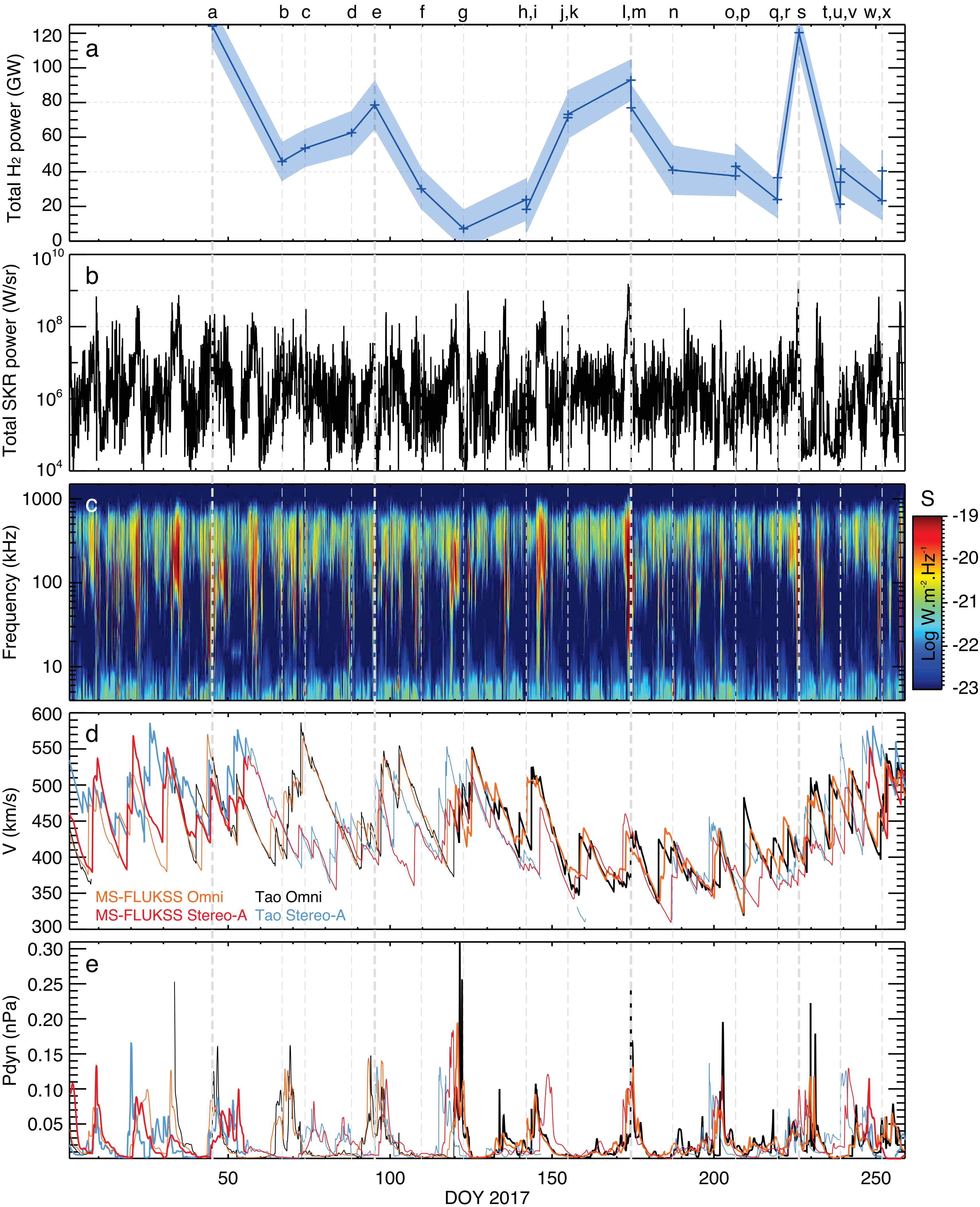
a
b
c
d
e
f
g
h,i
j,k
l,m
n
o,p
q,r
s
t,u,v
w,x
Total H2 power (GW)
Total SKR power (W/sr)
Frequency (kHz)
S
Log W.m-2.Hz-1
V (km/s)
MS-FLUKSS Omni
MS-FLUKSS Stereo-A
Tao Omni
Tao Stereo-A
Pdyn (nPa)
DOY 2017

Figure 3.

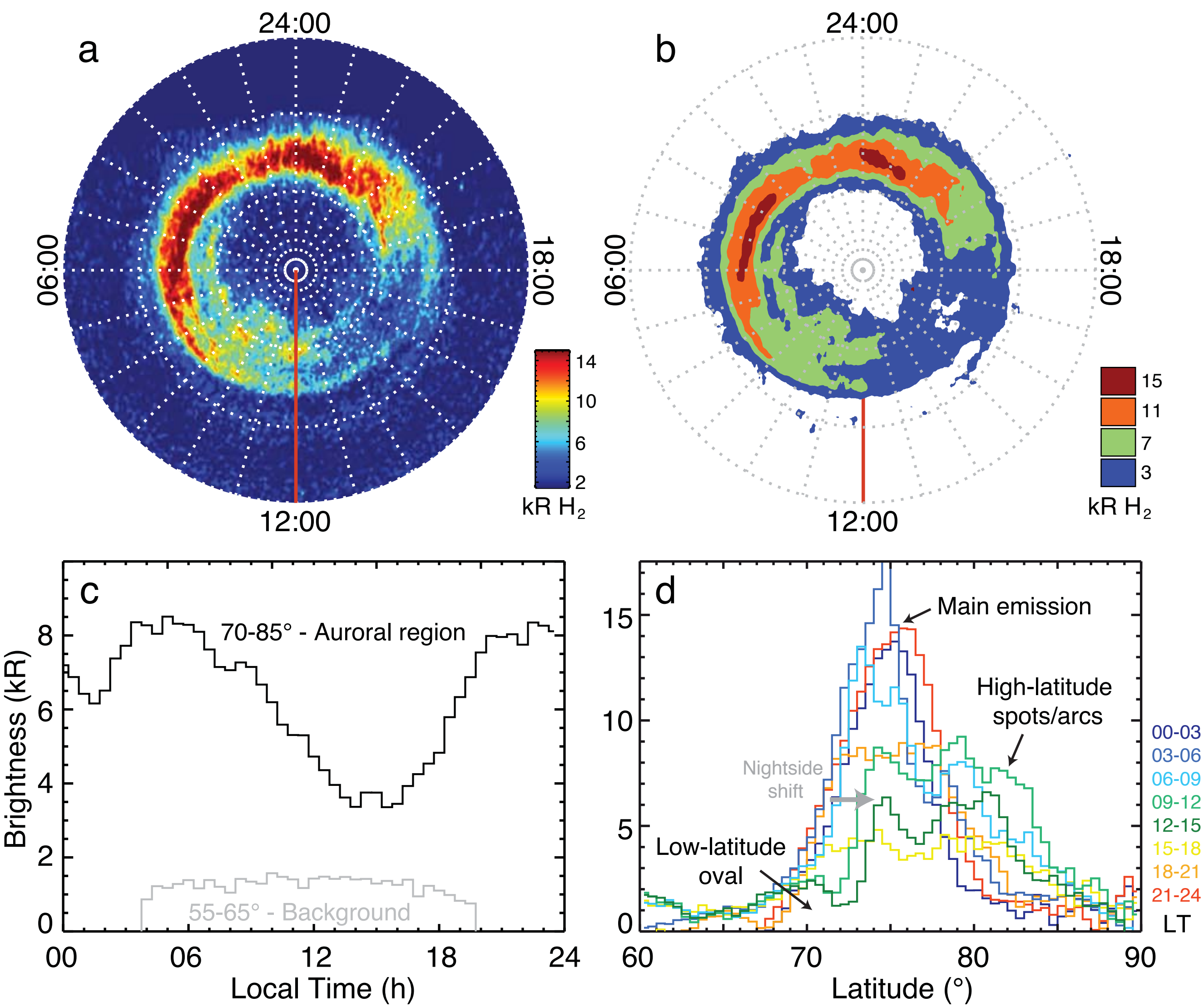

a
b
c
d
24:00
06:00
18:00
12:00
14
10
6
2
kR H2
15
11
7
3
kR H2
70-85° - Auroral region
55-65° - Background
Brightness (kR)
Local Time (h)
00
06
12
18
24
0
2
4
6
8
Main emission
High-latitude spots/arcs
Nightside shift
Low-latitude oval
00-03
03-06
06-09
09-12
12-15
15-18
18-21
21-24
LT
Latitude (°)
60
70
80
90
0
5
10
15

Supplemental Figure S2.

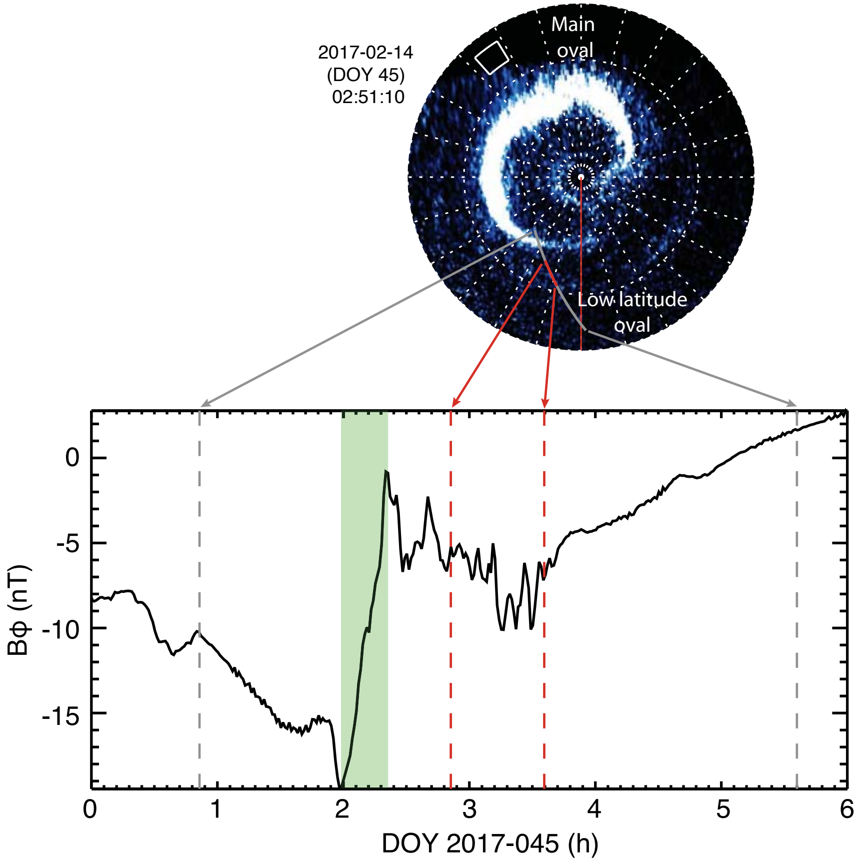
2017-02-14
(DOY 45)
02:51:10
Main oval
Low latitude oval
BΦ (nT)
0
-5
-10
-15
0
1
2
3
4
5
6
DOY 2017-045 (h)